Electronic Supplementary Information

Mass-transport-controlled, large-area, uniform deposition of carbon nanofibers and their application in gas diffusion layer of fuel cells

Xian Tang [a], Zhiyong Xie [a,*], Qizhong Huang [a,*], Guofen Chen [a], Ming Hou [b], Baolian Yi [b]

[a] State Key Laboratory for Powder Metallurgy, Central South University, 932 Lushan South Road, Changsha 410083, China

[b] Laboratory of Fuel Cells, Dalian Institute of Chemical Physics, Chinese Academy of Sciences, 457 Zhongshan Road, Dalian 116023, China

* E-mails: xzy507@csu.edu.cn; qzhuang@csu.edu.cn

1. Fabrication and Characterization of CP

A polyacrylonitrile (PAN)-based short-cut carbon fiber preform (Toray T−700) was impregnated in a solution of phenolic resin and ethanol for the fabrication of the CP substrate. After air-drying in a fume cupboard, the impregnated carbon fiber preform was dried in an oven at 80 °C for 1 h. The CP prepreg was molded using a flat vulcanizing machine at 3 MPa for 1 h to induce the curing reaction and then heat treated at 2000 °C for 1 h.

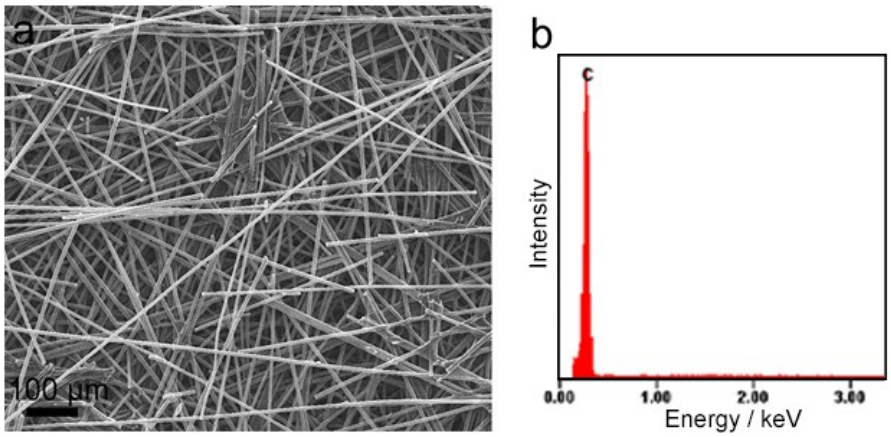

Figure S1. (a) SEM image and (b) EDS results of the CP used for CNF growth.

As shown in the SEM image presented in Figure S1a, the prepared CP consisted of carbon fibers as the main component and carbon resin as the binder. The CP had a density of 0.44 g cm^{-3} and a thickness of 0.194 mm. Macropores were generally observed in the CP. EDS results (Figure S1b) indicated that the CP contained no impurity elements.

Mechanical tests of the CP were performed using an Instron 3369 mechanical testing machine. The tensile strength was measured in accordance with the ASTM D828 test standard at a loading rate of 0.1 mm min^{-1}. The tensile strength σ of the specimen was calculated as follows:

$$\sigma = \frac{F}{w \cdot d}, \tag{1}$$

where F is the yield load and w and d are the width and thickness of the CP specimen, respectively.

Flexural tests were performed using the three-point bending configuration at a loading rate of 0.5 mm min^{-1}, in accordance with the BS ISO178 test standard. The flexural strength σ' was calculated using the following formula:

$$\sigma' = \frac{3F \cdot L}{2w \cdot d^2}, \tag{2}$$

where L is the fulcrum span.

The values obtained for σ and σ' were 17.89 and 41.85 MPa, respectively, guaranteeing that the integrity of the CP would be preserved during the CVD process.

The porosity of the CP products was determined based on Archimedes' principle in accordance with the ASTM C373 standard. The porosity was calculated using the following formula:

$$P = \frac{\rho_{water}(m_2 - m_1)}{\rho_{paraffin}(m_2 - m_3)} \times 100\%, \tag{3}$$

where P is the porosity; ρ_{water} ($\rho_{paraffin}$) is the density of water (paraffin); and m_1, m_2, and m_3 are the weights of the sample after drying in atmosphere, saturation with paraffin, and saturation with paraffin in water, respectively.

The permeability of the CP samples was characterized using an FBP-3Ⅲ porous material properties detector and was calculated using the following formula:

$$G = \frac{Q \cdot \mu \cdot d}{\Delta p \cdot S}, \quad (4)$$

where G is the gas permeability of the CP, Q is the ventilation volume per unit time, μ is the dynamic viscosity of the test gas (air), Δp is the pressure difference across the CP specimen, and S is the area of the specimen.

The values obtained for P and G for the CP were 72.1% and 8.833×10^{-12} m^2, respectively, confirming that the gases would be able to diffuse into the pore channels of the CP to decrease the pressure difference between the two sides.

2. CFD Simulations

2.1 Model and Boundary Conditions

The experimental CVD reactor (schematically depicted in Figure 1b) was modeled as a 2D rectangular channel with a width of 15 cm and a height of 50 cm, corresponding to the actual geometry. The gases were delivered at the bottom inlet and flowed to the top outlet. The two sides were modeled as reactor walls whose inner and outer sides were adiabatic. The initial constant velocity of the C_3H_6/N_2 flow (mass fraction of 0.13/0.87 and temperature of 973 K) was calculated to be 0.01 m s^{-1}, based on the experimental flow rate and the cross-sectional area of the inlet. The walls were considered to be a constant heat source to maintain the modeled substrate at the CNF growth temperature of ~973 K. The no-slip boundary condition was assumed on the walls. The 2D porous CP substrate was simplified to a 1D porous-jump medium (12 cm), imposing a pressure drop across the substrate and ignoring the internal structural characteristics [1]. The medium was placed at the center of the channel at an incline consistent with the experimental α.

2.2 Calculation Method

Using the finite-volume method, the model geometry with the applied boundary conditions was divided into discrete control volumes to compute the velocity, pressure, temperature, and concentration profiles in the reactor. The reactor models, in each of which a porous-jump medium was embedded to represent the substrate, were meshed with quadrilateral cells; the total numbers of cells were 117,688, 135,718, 117,630, 120,320 and 117,688 for α = 0°, 22.5°, 45°, 67.5° and 90°, respectively. Because we focused on the field distribution profiles at the substrate surface and for the purpose of clarity, only the meshes near the substrate models are shown in Figure S2.

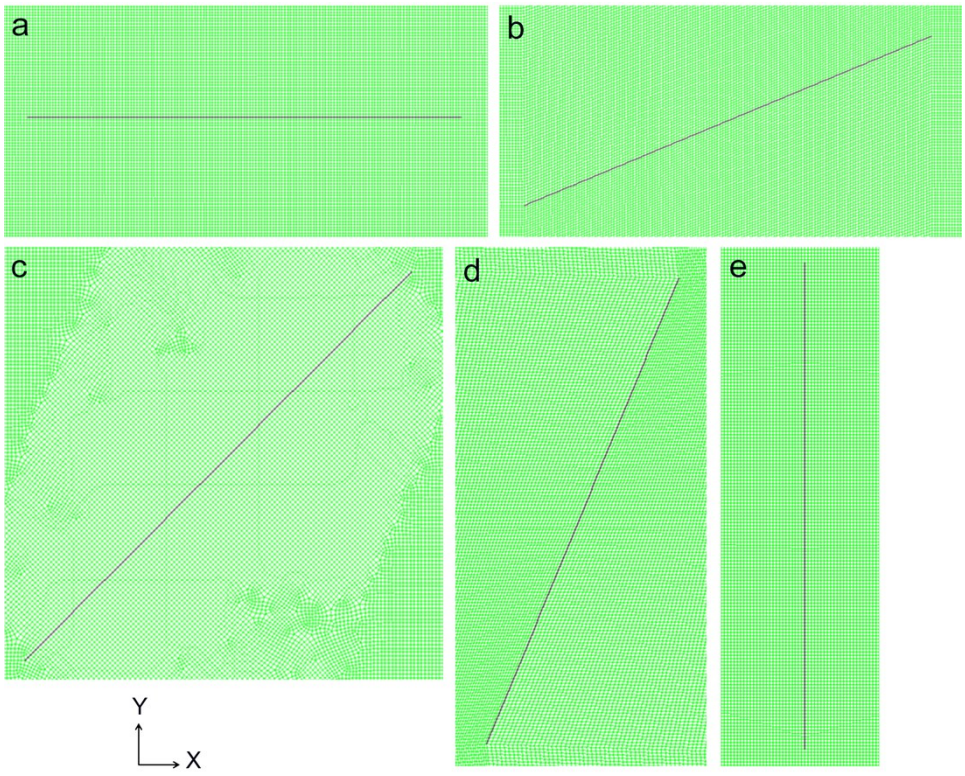

Figure S2. Meshes near the porous-jump media (represented by the black lines) used for CFD calculations at (a) α = 0°, (b) α = 22.5°, (c) α = 45°, (d) α = 67.5° and (e) α = 90°. X and Y denote the directions along the width and height of the reactor, respectively.

The gas mixture in the reactor was assumed to be an ideal compressible gas. The effects of radiation, pressure diffusion, forced diffusion, and viscous heating were neglected. The governing equations for the conservation of mass, momentum, energy, and species are as

follows.

The continuity equation is

$$\nabla \cdot (\rho \boldsymbol{u}) = 0, \tag{5}$$

where ρ is the density of the gas mixture and $\boldsymbol{u}$ is the local velocity vector.

The Navier–Stokes equation is

$$\nabla \cdot (\rho \boldsymbol{u}\boldsymbol{u}) = -\nabla p + \nabla \cdot (\bar{\bar{\tau}}) + \boldsymbol{S}, \tag{6}$$

where p and $\bar{\bar{\tau}}$ [2] are the pressure and the shear stress tensor, respectively. $\boldsymbol{S}$ [3] is the momentum source term associated with the presence of the porous medium. In the porous-jump model, this term is modified by applying a pressure drop ($\Delta p'$) across the porous boundary:

$$\Delta p' = -d\left(\frac{\mu'}{G} v + \frac{1}{2} C \rho v^2\right), \tag{7}$$

where μ' is the fluid viscosity, G (8.833×10^{-12} m^2) is the gas permeability of the CP, and v is the velocity normal to the surface of the medium. At low flow velocities, the Reynolds number was estimated to be less than 1200, and the variation in the pressure drop with the velocity through the CP tended to be linear during the permeability tests. Therefore, the gas flow was considered to be laminar, following Darcy's law, and the inertial resistance factor C was set to 0.

The convection–diffusion equation for energy conservation is

$$\nabla \cdot (\rho C_p \boldsymbol{u} T) = \nabla \cdot (k_{eff} \nabla T) - \nabla \cdot \left(\sum_{i=1}^{n} h_i \boldsymbol{J_i}\right) + S_h, \tag{8}$$

where C_p is the specific heat capacity at constant pressure, T is the temperature, and k_{eff} [4] is the effective thermal conductivity. h_i and $\boldsymbol{J_i}$ are the enthalpy and diffusion flux of species i, respectively. S_h is the heat source term originating from chemical reactions, which were simulated using the laminar finite-rate model. In this study, the free-radical chain mechanism of C_3H_6 pyrolysis at low temperatures [5] was incorporated into the simulation of mass

transport. Nine reactions were involved in this mechanism. The A factor and activation energy were fitted using the Arrhenius equation for three-halves-order rate constants, which were calculated from the H_2/C_3H_6 molar ratio that was measured after C_3H_6 pyrolysis using a gas chromatograph [6].

The mass transfer equation is

$$\nabla \cdot (\rho \boldsymbol{u} y_i) = -\nabla \cdot \boldsymbol{J_i} + M_i \cdot \sum_{k=1}^{N_k} R_{i,k}, \quad (9)$$

where y_i and M_i are the mass fraction and molecular weight of species i. $N_k = 9$ is the number of volumetric reactions. $R_{i,k}$ is the Arrhenius molar rate of creation/destruction of species i in reaction k.

The governing equations were solved using the FLUENT 6.3.26 commercial code with a segregated pressure-based solver. All calculations were performed in the steady state. The first-order upwind scheme was used to discretize the convection term in the transport equations. The pressure–velocity coupling was solved using the standard SIMPLE algorithm. A convergence criterion of 10^{-3} was applied to the residuals of the continuity, momentum, and species equations, and a criterion of 10^{-6} was applied to the residual of the energy equation. The calculations were iterated until the convergence criteria were achieved.

2.3 Model Validation

The model was verified by comparing the experimental and simulated temperature profiles near the substrate surface at α = 22.5°. As shown in Figure S3, the simulated 2D profile exhibited a temperature gradient from the reactor wall to the surface of the porous medium (indicated by the black line) because of the heat consumption of the fluid flux. The temperature boundary layer changed along the inclined surface of the medium. To effect a comparison, the data from a column of points in the profile (indicated by the black dashed line) were recorded, and temperature measurements were conducted at the corresponding positions in the CVD reactor. It is evident in Figure S3 that the simulated and measured data

exhibited similar variations with the Y position, whereas discrepancies are present in the regions of relatively low and high temperatures. However, these discrepancies are within a reasonable range of ±20 K, thereby confirming good agreement between the calculations and the experiments. The simulations indicated that the range of the temperature fields did not change significantly with α, and therefore, similar agreement for α = 0°, 45°, 67.5° and 90° can be deduced.

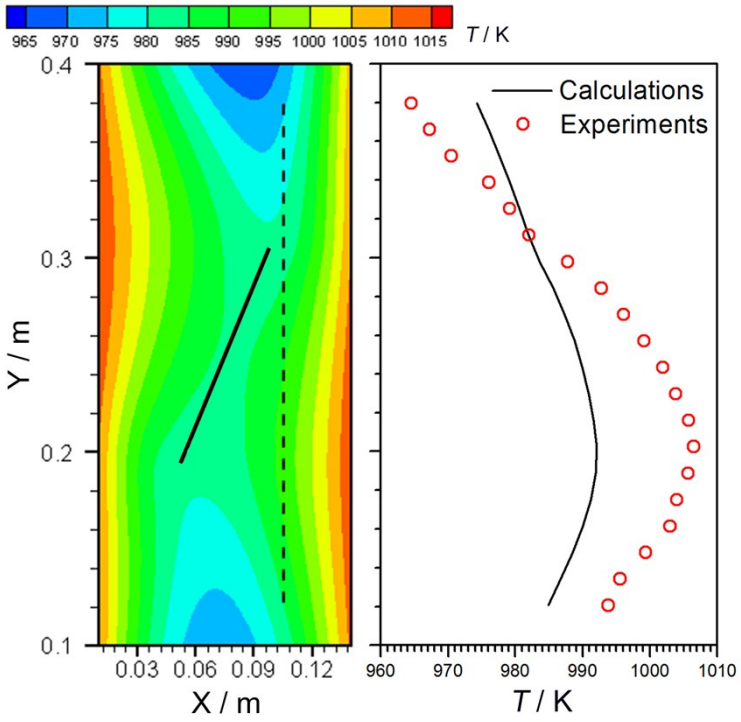

Figure S3. Left: Temperature distribution of the simulated 2D reactor. The X and Y positions correspond to the width and height of the reactor, respectively, from end to end. The solid and dashed black lines represent the porous-jump medium and the positions used for extraction of the calculated data, respectively. Right: Comparison of the extracted and measured data.

3. Supplementary Figures

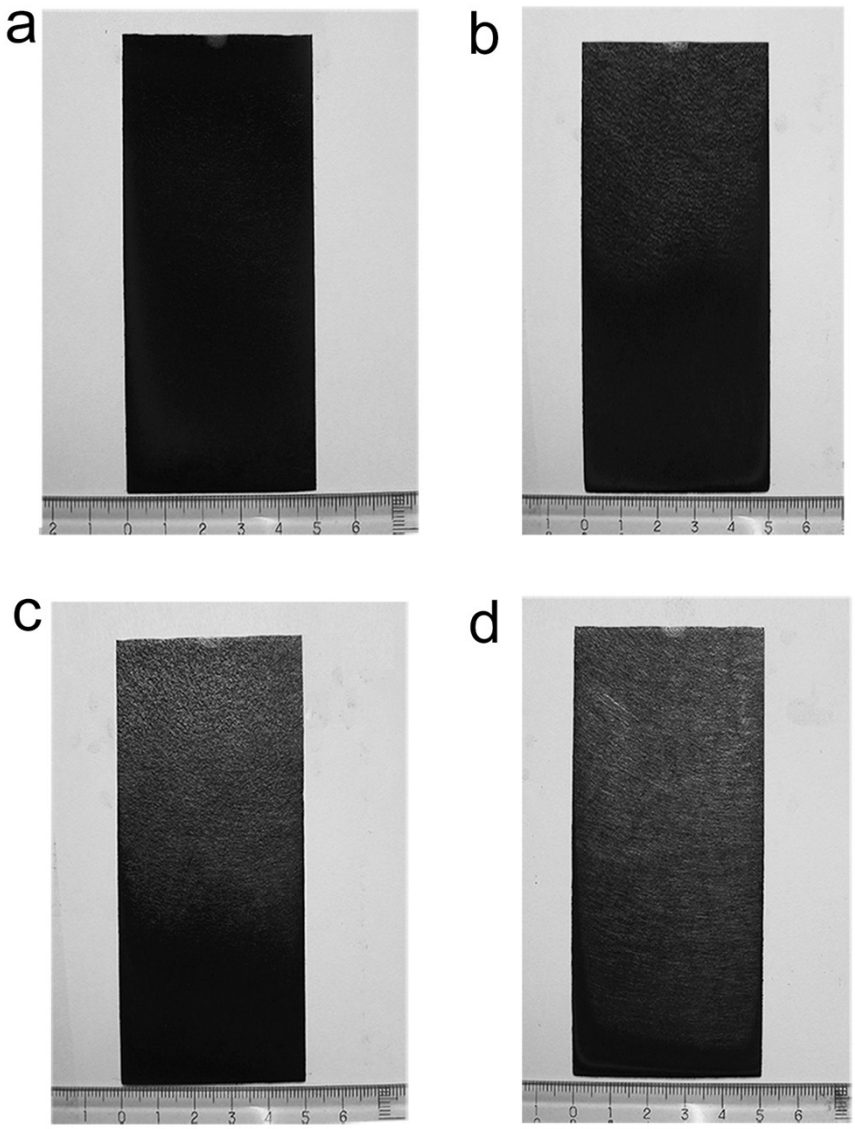

Figure S4. Optical images of CNFs grown on CP at various deposition angles: (a) α = 22.5°, (b) α = 45°, (c) α = 67.5° and (d) α = 90°. The dark regions in the samples represent the CNFs, and the light regions represent the CP substrate.

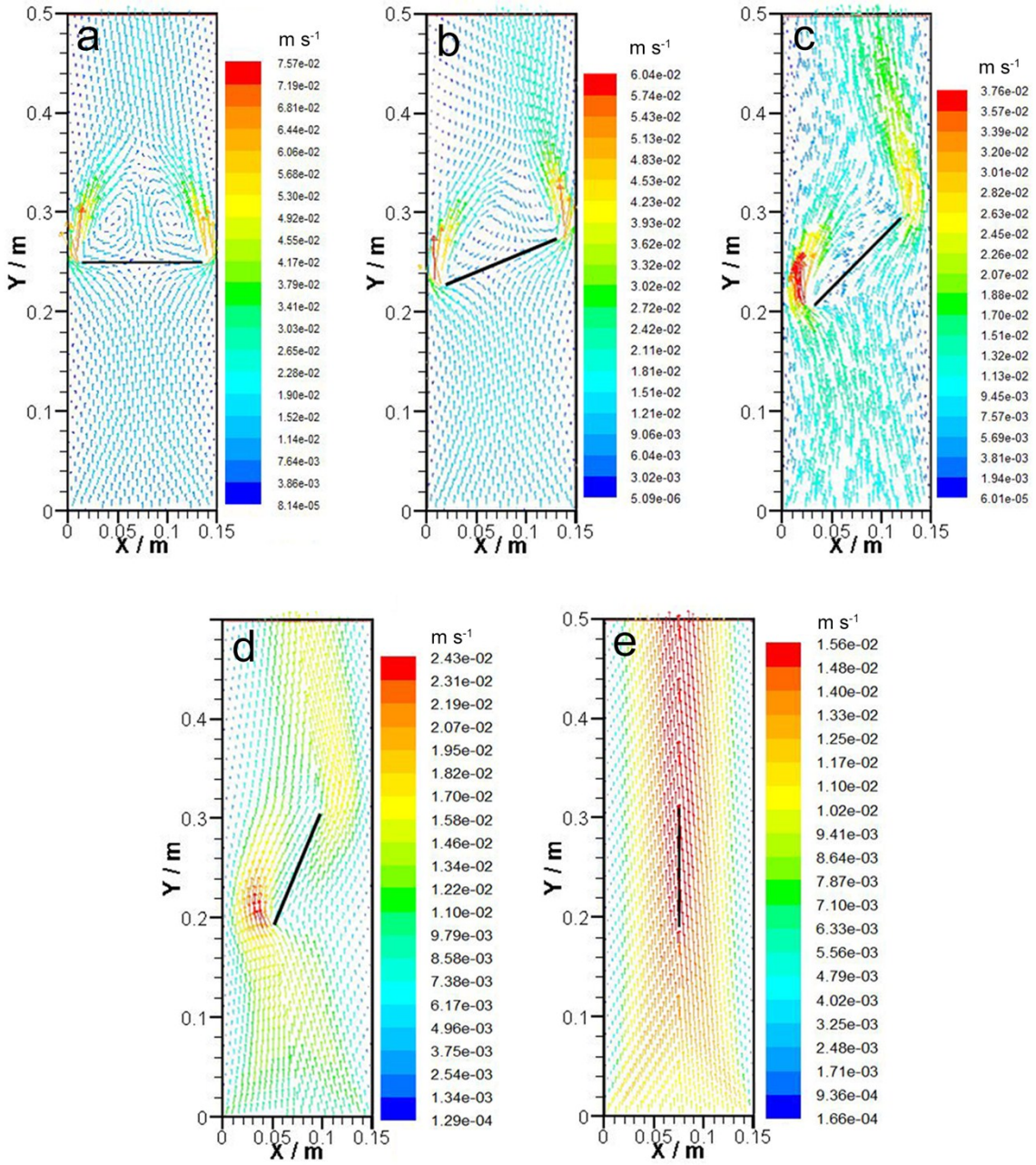

Figure S5. Modeled velocity profiles in the CVD reactor with the modeled porous substrate medium (represented by the black lines) inclined at (a) $\alpha = 0°$, (b) $\alpha = 22.5°$, (c) $\alpha = 45°$, (d) $\alpha = 67.5°$ and (e) $\alpha = 90°$.

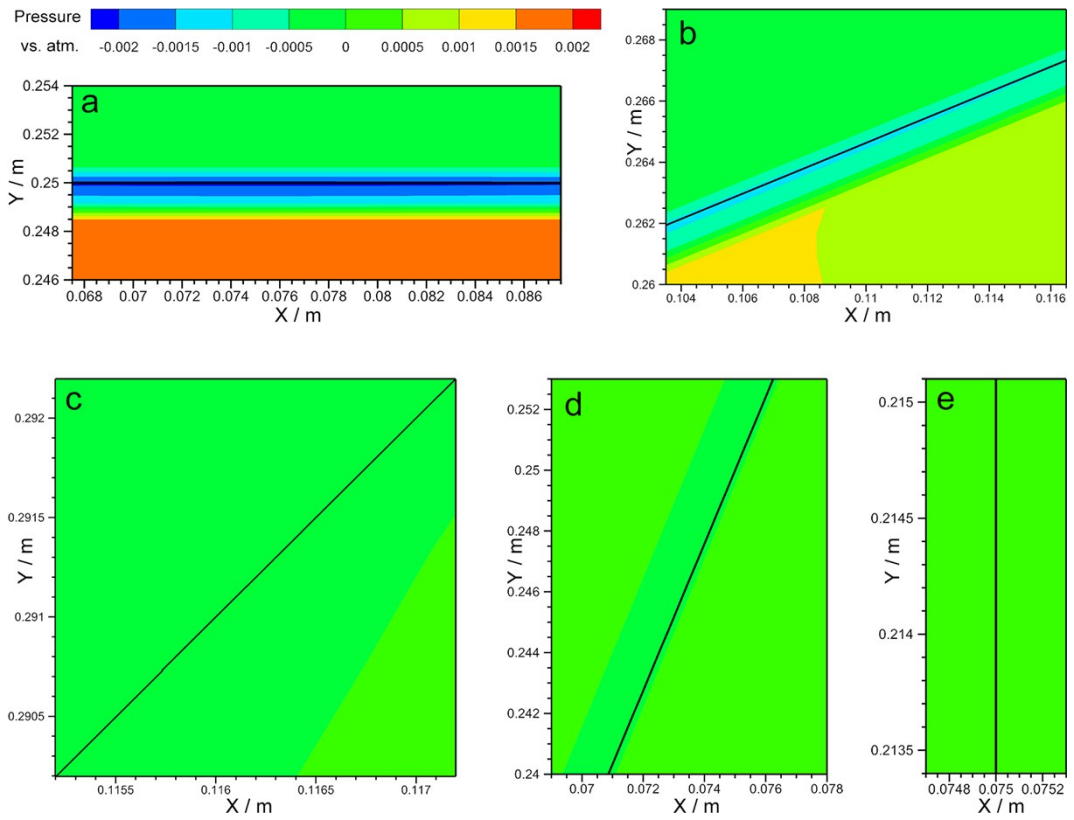

Figure S6. Pressure profiles in the CVD reactor with the modeled porous substrate medium (represented by the black lines) inclined at (a) $\alpha = 0°$, (b) $\alpha = 22.5°$, (c) $\alpha = 45°$, (d) $\alpha = 67.5°$ and (e) $\alpha = 90°$. A marked uniform pressure boundary layer was created on the lower surface of the medium at $\alpha = 0°$. The pressure gradient on the lower surface decreased with increasing α and became negligible at $\alpha \geq 45°$.

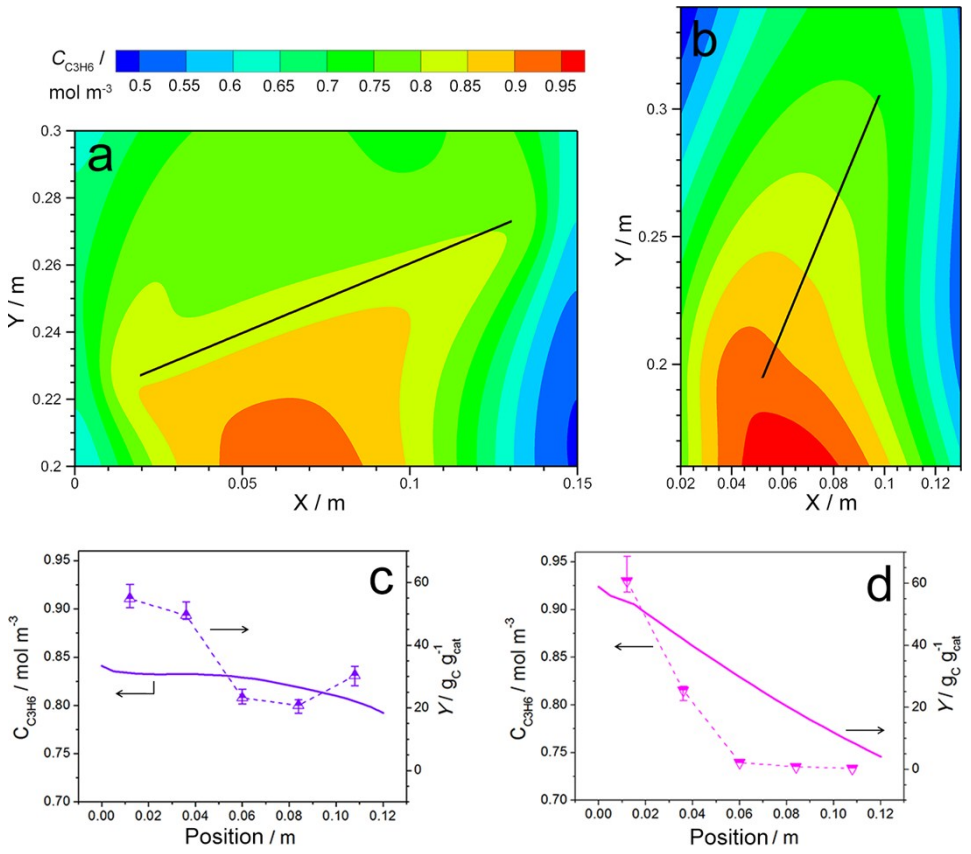

Figure S7. Profiles of the C_{C3H6} distributions near the porous media (indicated by the black lines) at (a) α = 22.5° and (b) α = 67.5°. Also shown are the variations of C_{C3H6} extracted from the surface of the medium and the experimentally measured values of Y with substrate position at (c) α = 22.5° and (d) α = 67.5°. C_{C3H6} decreased from 0.84 to 0.79 mol m^{-3} as Y decreased from 54.8 to 20.8 g_C g_{cat}^{-1} at α = 22.5°; C_{C3H6} decreased from 0.92 to 0.75 mol m^{-3} as Y decreased from 60.8 to 0.3 g_C g_{cat}^{-1} at α = 67.5°.

Table S1. Fit parameters using the equivalent circuit model shown in Figure 7 for single PEMFCs with different MPLs.

MPL	R_Ω (Ω cm^2)	R_{ct} (Ω cm^2)	R_{mt} (Ω cm^2)
Uniform CNF film	0.23	0.23	0.02
Non-uniform CNF film	0.44	0.21	0.08
Vulcan XC-72	0.32	0.22	0.03

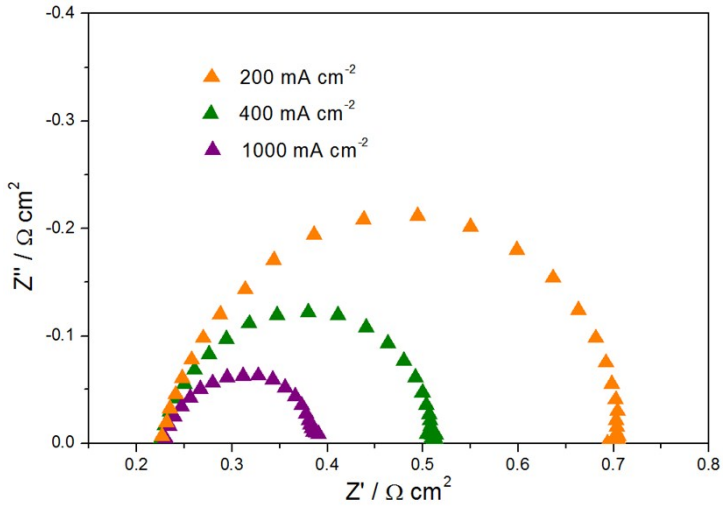

Figure S8. Nyquist plots for the single cell fabricated using a uniform CNF film at different current densities.

References

[1] ANSYS FLUENT User's Guide Release 13.0. FLUENT Inc; 2010, p. 337–9.

[2] Tsai ML, Fang CC, Lee LY. Numerical simulation of the temperature distribution in a planetary MOCVD reactor. Chem Eng Process 2014;81:48–58.

[3] Mishra P, Verma N. A CFD study on a vertical chemical vapor deposition reactor for growing carbon nanofibers. Chem Eng Res Des 2012;90:2293–301.

[4] Lin CH, Cheng WT, Lee JH. Effect of embedding a porous medium on the deposition rate in a vertical rotating MOCVD reactor based on CFD modeling. Int Commun Heat Mass Transf 2009;36:680–5.

[5] Amano A, Uchiyama M. Mechanism of the pyrolysis of propylene: the formation of allene. J Phys Chem 1964;68:1133–7.

[6] Amano A, Uchiyama M. Thermal hydrogesolysis of propylene. J Phys Chem 1963;67:1242–7.